Applied Catalysis B: Environmental 331 (2023) 122693

Contents lists available at ScienceDirect

Applied Catalysis B: Environmental

journal homepage: www.elsevier.com/locate/apcatb

When copper is not enough: Advantages and drawbacks of using copper in de-NOx reactions over lanthanum manganite perovskite structures

Christoph W. Thurner [a], Xaver Drexler [a], Leander Haug [a], Daniel Winkler [a], Julia Kunze-Liebhäuser [a], Johannes Bernardi [b], Bernhard Klötzer [a], Simon Penner [a,*]

[a] Department of Physical Chemistry, University of Innsbruck, Innrain 52c, A-6020 Innsbruck, Austria
[b] Technische Universität Wien, USTEM / 057–02, Wiedner Hauptstr. 8–10, A-1040 Wien, Austria

ARTICLE INFO

Keywords:
Exsolution
Electron microscopy
Alloying
NO reduction
Humid

ABSTRACT

Using a Cu-doped lanthanum manganite perovskite structure ($LaCu_{0.5}Mn_{0.5}O_{3-\delta}$), we show how Pd addition following different synthesis approaches (sol-gel vs. impregnation) allows to overcome the oxidation limitation of Cu in realistic de-NO_x reaction mixtures involving NO, CO, O_2 and water. The beneficial interplay of Cu with the oxygen-deficient perovskite resulting from in situ exsolution during humid de-NO_x treatments is strongly connected with the metallic Cu state enhancing the N_2O chemistry. The beneficial catalytic properties of metallic Cu can be preserved by adjustment of the Pd amount, as evidenced by combined in situ X-ray photoelectron spectroscopy and catalytic experiments following the main reactions of the de-NOx reaction network, including water-gas shift reaction and CO oxidation. The concept of impregnation with a noble metal and simultaneous exsolution with Cu yields a reactive Cu(Pd)/perovskite interface and provides a first step towards the economization of the noble metal content at the surface in future works.

1. Introduction

The reduction of NO by CO to elemental N_2 (1) is a prominent model reaction for a variety of technological processes, such as the denitrification (de-NO_x) of exhaust gas from combustion mixtures using air as oxidant.

$$2NO_{(g)} + 2CO_{(g)} \rightleftharpoons N_{2(g)} + 2CO_{2(g)} \quad (1)$$

The partial reduction of NO also causes the formation of N_2O, a greenhouse gas and cause of stratospheric ozone depletion, with a global warming potential of 265 CO_2 equivalents and an atmospheric lifetime of 121 years [1]. The model reaction (2).

$$N_2O_{(g)} + CO_{(g)} \rightleftharpoons N_{2(g)} + CO_{2(g)} \quad (2)$$

describes the reductive degradation of N_2O, which is emitted e.g., during nitric and adipic acid production [2] and in the polymer industry [3].

A main issue in general de-NO_x research concerns the impact of parasitic side reactions on catalytic materials in the presence of water, which is an important component in model exhaust gas mixtures. The most prominent is the water-gas shift (WGS) reaction (3).

$$H_2O_{(g)} + CO_{(g)} \rightleftharpoons H_{2(g)} + CO_{2(g)} \quad (3)$$

The key step of this reaction is the activation, i.e., splitting of water. The necessary formation of H_2 or H_{ads} in this pathway causes highly reductive conditions, which in consequence leads to the full reduction of NO to NH_3, which is frequently observed on supported noble metals [4–6].

State-of-the-art catalytic materials, such as supported noble metals (e.g., Rh, Pt or Pd [7]), compete with perovskite-based compounds (main stoichiometry ABO_3), which are under investigation for several decades [8]. Initially, perovskites based on $LaCoO_3$ were reported to rival Pt [9] and subsequently, their possible application for automotive emission control was studied [10]. Noble metals were also investigated as structural and chemical dopants in a variety of perovskite structures for automotive exhaust gas treatment [11,12]. In this respect, the bifunctionally operating Pd/perovskite interface was suggested as a prominent catalyst candidate for the NO reduction reaction, at least under dry conditions [13–16].

Considering chemical aspects regarding NO activation (reaction 1), oxygen deficient metal oxides, such as perovskites, serve as promoter in activating the NO bond [17]. With respect to the decomposition of N_2O (reaction 2, and therefore pushing the selectivity toward N_2), Cu is

* Corresponding author.
E-mail address: simon.penner@uibk.ac.at (S. Penner).

https://doi.org/10.1016/j.apcatb.2023.122693
Received 13 December 2022; Received in revised form 23 March 2023; Accepted 24 March 2023
Available online 27 March 2023

considered a promising candidate in enhancing this particular reaction pathway [18,19]. Supported Cu catalysts exhibit low-temperature water-gas shift activity (≈200 °C) [20], therefore reaction 3 deserves special consideration. One strategy to suppress parasitic WGS reactions is to withdraw CO from the reaction equilibrium by oxidation with O_2 (reaction 4) at a lower temperature regime compared to the WGS-reaction (3). In this perspective, Cu/perovskite interfaces have been shown to provide high activity in CO oxidation [21].

$$2CO_{(g)} + O_{2(g)} \rightleftharpoons 2CO_{2(g)} \quad (4)$$

The main drawback of metallic Cu is the poor oxidation stability in oxidizing atmospheres, which also includes H_2O steam as an excess component in technologically relevant de-NO_x applications.

A concept combining the discussed approaches, in addition to providing the huge benefit of sinter-stability [22], is metal exsolution from perovskites [13–16,22–26]. We have shown in two recent works, how control of the Pd and Cu/lanthanum perovskite interface enables the exact tuning of the de-NO_x activity [27,28] and in particular, how Cu is in principle able to replace noble metals in a model NO+CO reaction [28]. We relied on the parent perovskite material $LaMnO_3$, as it serves as a temperature-stable active structure [29]. By B-site substitution of manganese in $LaMnO_3$ with copper, oxygen defects are generated [30,31], fulfilling the requirement of oxygen deficiency in order to activate NO. Theoretical calculations show that Cu doping of $LaMnO_3$ improves the reducibility of the parent $LaMnO_3$ structure [32], thereby promoting the reductive exsolution of metallic copper particles. This approach thus far, however, does not solve the problem of deactivation by (intermediate) copper oxidation, as even oxygen spillover from the oxygen-deficient perovskite structure is plausible under dry de-NO_x conditions. This has been shown recently for Ni-based perovskite materials [33]. We anticipate also the effect of oxidation by water under realistic de-NO_x reaction conditions, but also to overcome this problem by doping the LCM structure with minute amounts of Pd. During the NO+CO treatment, co-exsolution of both copper and palladium occurs, leading to alloyed and surface-bound Cu-Pd particles. We expect to steer and control the oxidation behavior of copper by controlling the amount of Pd within the exsolved copper particles. As the reduction of palladium oxide is facilitated in comparison to copper oxide [34], the co-exsolution of the respective lattice M^{2+} species is even enhanced by adding Pd^{2+}. Cu(0)-Pd(0) exsolution is therefore anticipated, yielding a potentially active, vacancy-doped and oxidation-stable Cu-rich Cu_xPd_y/perovskite interface. A second viable strategy to increase the nobility of Cu is to impregnate the LCM surface deliberately by Pd. Alloying the surface-abundant Pd with Cu during exsolution, thus, increases the Pd amount of the particles, establishing a comparatively Pd-richer Cu_xPd_y/perovskite interface. To investigate both, the promotional effect of Pd on the oxidation stability and catalysis and the catalytic effect of Cu itself, we prepared a pure $LaCu_{0.5}Mn_{0.5}O_{3-\delta}$ (termed LCM55 in the following) perovskite catalyst, its respective B-site doped variants $La(Cu_{0.5}Mn_{0.5})_{0.98}Pd_{0.02}O_{3-\delta}$ (y = 0.02) with 0.86 wt% Pd via a sol-gel method (termed SG) and a wet-impregnated LCM55 (termed IM) with the same Pd amount (0.86 wt%). To compare the temperature-dependent activity of each LCM55-based catalyst and to outline the benefits of the Cu_xPd_y/LCM55 interface in terms of stability, activity and selectivity we synthesized two reference catalysts by a wet-impregnation approach. Serving as a benchmark, the catalytic behavior of these references, the respective Cu-particles (7.0 wt%) and Pd-particles (0.86 wt%) on an inert support (silica) were investigated.

The main goal of the study is to unravel the advantages and drawbacks of using copper as exsolvable dopant to create a Cu/LCM interface under realistic humid de-NO_x conditions and to eventually overcome the limitation of deactivation by copper oxidation. As such, we also test this interface in the two important parasitic side reactions of water-gas shift reaction and CO oxidation, as the suppression of the former and potential enhancement of the latter appear very crucial in creating a reactive Cu/LCM interface with high activity and low-temperature nitrogen selectivity. We extend the studies also to more realistic exhaust gas conditions with excess water, CO and O_2, as this is anticipated to severely impact the product selectivity by formation/suppression of unwanted NH_3 and of oxidized vs. reduced Cu species. Structure-reactivity and -selectivity relationships will be established by correlating the catalytic performance to surface chemical changes monitored by in situ X-ray photoelectron spectroscopy under realistic de-NO_x conditions.

2. Experimental

2.1. Synthesis of the materials

A sol-gel self-combustion approach was followed to synthesize the B-site doped perovskite catalysts $La(Cu_{0.5}Mn_{0.5})_{1-y}Pd_yO_{3-\delta}$ (y = 0 and 0.02 ≙ 0.86 wt%). Stoichiometric amounts of metal nitrates were dissolved in de-ionized (DI) water, before glycine was added as a complexing agent in a molar ratio glycine/nitrate = 1. A sticky gel resulted after heating the solution to 80 °C under continuous stirring to remove excess water. Gel decomposition was induced by increasing the temperature to 250 °C and final self-ignition, yielding a black powder in a total yield of ~95%. The as-synthesized powder was calcined at 700 °C for 5 h in air. La$(NO_3)_3$·6 H_2O (Alfa Aesar, 99.9% (REO)), Mn$(NO_3)_2$·4 H_2O (Sigma Aldrich, 97.0% (KT), Cu$(NO_3)_2$·3 H_2O (Merck, 99.5%), Pd$(NO_3)_2$·2 H_2O (Sigma Aldrich, 99.9%) and glycine (Sigma Aldrich, 99.9%) were used for synthesis.

For wet-impregnation synthesis of 0.86 wt% Pd on LCM55, the freshly calcined LCM55 powder was suspended in deionized water and a solution of dissolved Pd-nitrate was added dropwise over the course of 30 min. After solvent removal by gentle evaporation, the obtained powder was dried at 120 °C for 24 h followed by calcination at 700 °C for 1 h in air, yielding the as-synthesized PdO_x/LCM55 material.

To evaluate the synergistically operating Cu_xPd_y/perovskite interface, we reference the catalytic activity and selectivity to the respective Cu-free, Pd-free and perovskite-free materials. Details of the synthesis of the reference catalysts (Cu/SiO_2 and Pd/SiO_2) are given in the Supporting Information (SI), App. A.

2.2. Structural and spectroscopic characterization

2.2.1. Transmission Electron Microscopy (TEM)

Chemical and structural analysis was performed using a FEI Tecnai F20 microscope operated at 200 keV and equipped with a SDD-EDX TEAM Apollo XLTW detector. For the measurements, the powder samples were placed on holey carbon films without further treatment.

2.2.2. Powder X-Ray Diffraction (PXRD)

All ex situ XRD measurements were performed in transmission mode utilizing a STOE Stadi-P diffractometer, equipped with a DECTRIS MYTHEN2 DCS4 detector and a Mo X-ray tube (GE Sensing & Inspection Technologies GmbH, Ahrensburg, Germany). All diffractograms were collected using Mo $K_{\alpha1}$ radiation with a wavelength of $\lambda = 0.7093$ Å. The WinXPOW software and the ICDD and ICSD databases were used for qualitative analysis.

2.2.3. Near Ambient Pressure X-ray Photoelectron Spectroscopy (NAP-XPS)

In situ X-ray photoelectron spectra were collected using a custom-made SPECS X-ray photoelectron spectroscopy setup. A detailed description of the experimental setup is given in the SI, App. B. During all the experiments the gas atmosphere consisted of a mixture of NO and CO with and without H_2O vapor (ratio 1:1:(1); 0.3 mbar each; CO: Messer, Purity 4.7; NO: Linde, Purity 2.5; H_2O: vapor from deionized water, Merck, ultra-pure Milli-Q 18.2 MΩ). The main interest of the NAP-XPS investigation is to observe changes of the surface oxidation

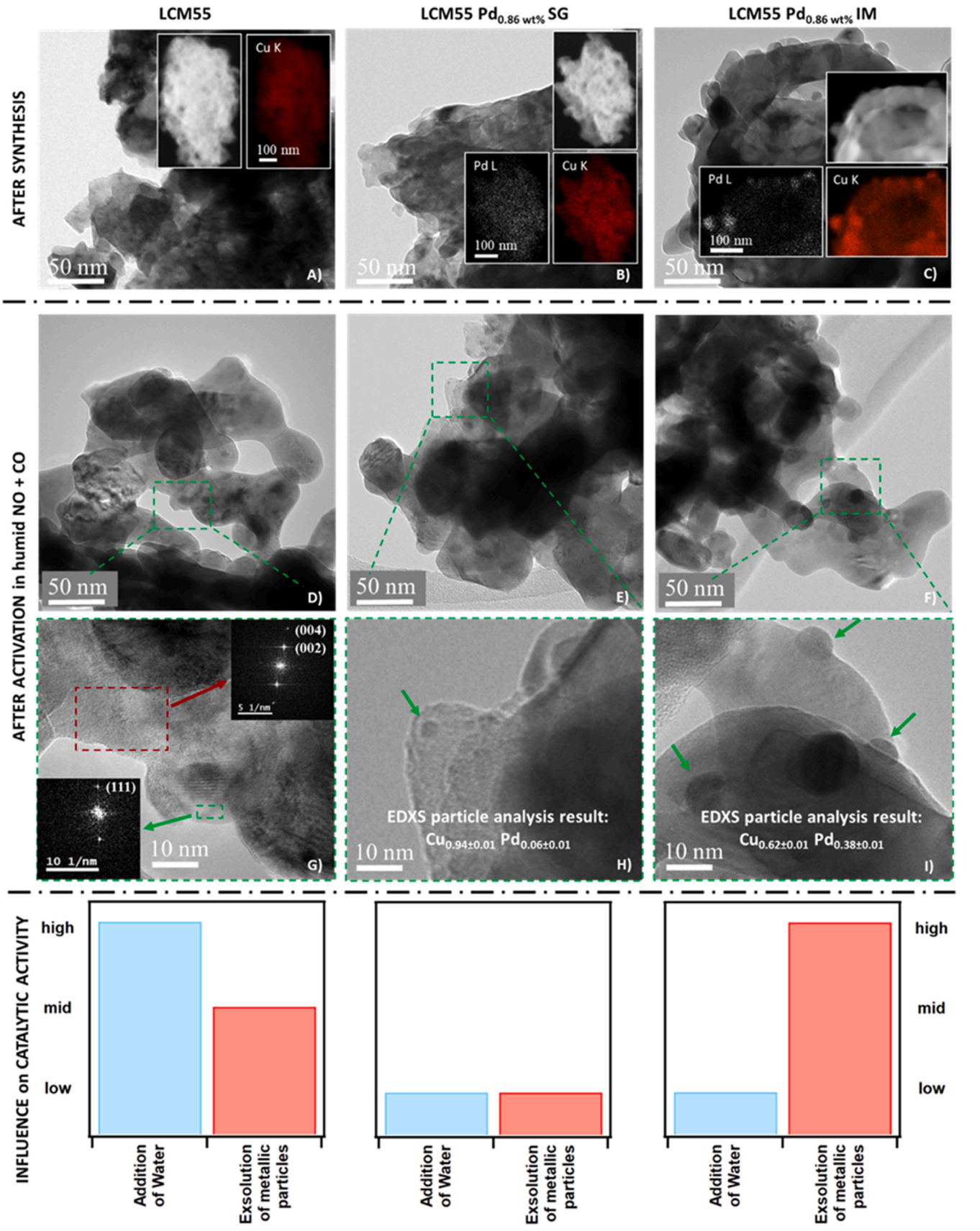

(caption on next page)

Fig. 1. Electron microscopy analysis of pure LCM55 (left), Pd-doped LCM55 obtained a via sol-gel route (middle) and Pd-impregnated LCM55 (right), separated into imaging after synthesis (top row) and after the pre-activation step (overview images: middle row, detailed images: bottom row). Panels A-C show overview images of the respective catalysts. Panel D and G depict high-resolution images of LCM55 and of an isolated exsolved Cu(0) particle. Fast Fourier Transform shown as insets. Identical location EDX line scan analysis exclusively identifies Cu (SI, App. I, Fig S6). Panel H shows an enlargement of the image highlighted in Panel E. On the green-arrow-marked particles EDX area analysis were carried out resulting in an averaged composition of the particles of $Cu_{0.94\pm0.01}Pd_{0.06\pm0.01}$. Panel F and I show HRTEM images of 0.86 wt% Pd-impregnated LCM55. The EDX area analysis result in an averaged particle composition of $Cu_{0.62\pm0.01}Pd_{0.38\pm0.01}$. For details regarding the particle composition we refer to the SI, App. I, Fig S7 and App. J, Table S6. The bar graph panels schematically show the influence of both the addition of water vapor to the reaction mixture and the formation of metallic particles via exsolution on the catalytic activity.

state of Cu during the catalytic treatments. Therefore, Cu compounds (Cu, Cu_2O and CuO) with Cu in the oxidation states (0), (I) and (II) serve as reference materials to limit the constraints (e.g., peak position and full-width-at-half-maximum) used in the peak fitting procedure. The measured XP-spectra od the $Cu2p_{3/2}$ and Cu LMM region and a table summarizing the results derived are given in the SI, App. C in Fig. S1 and Table S1. As for the assignment of the chemical shifts, we note that for Cu divalent ions, the maximum energy values of the resulting XP peaks can exist over a wide range depending on their coordination states (such as $Cu(OH)_2$ or CuO). Although this feature is also present for monovalent and metallic Cu, the energy range for Cu^+ and Cu^0 is typically narrower compared to Cu^{2+}. This feature has been accounted for in the framework of the discussion of Figs. 2 and 6.

2.3. Catalytic experiments

The evaluation of the catalytic data is based on a combined mass spectroscopy and Fourier transform infra-red spectroscopy online measurement of the downstream gas-phase. An explanation in how activity rates are calculated from these experiments is pointed out in detail in the SI, App. D in Figs. S2 and S3. As we expect to induce structural changes in the catalyst during the catalytic treatments, we relied on the determination of the mass-specific activity (mol s^{-1} g^{-1}) derived from the contact time to the catalyst bed for rate/activity calculations. As we aim to investigate catalysts with minute amounts of Pd, the Pd-content (0.86 wt.-%) was kept the same over all catalysts (LCM-based and reference). Therefore, only the mass-specific activity rates allows ensuring comparability of the different samples. No substantial variation of the BET surface area (SI, App. E, Table S2) has been observed, supporting the normalization to the catalyst mass. The surface area scattering of the LCM55-based samples is a consequence of synthesis influenced by Pd-doping vs. Pd-impregnation. Based on that fact, the reference catalysts were synthesized using a respective support material with a surface area in range of the LCM-based samples.

To give a semi-quantitative account of the reaction kinetics and the catalytic data, we combined determination of both the activation energy (E_a) and the pre-exponential factors (derived from the Arrhenius fits of the initial consumption rates at low conversion) with the particle coverage estimation (derived from the analysis of the La3d and Cu2p XPS data via an attenuated overlayer model [35] extended for fractional coverage by particles). For details we refer to the SI, App. F, Fig. S4 and Tables S3 and S4.

For the humid NO+CO reaction, the catalysts were heated at 2 °C min^{-1} from 50 °C to 500 °C in a gas mixture of 1% NO (Linde, Purity 4.5), 1% CO (Linde, Purity 4.5) and 1% H_2O. All cited concentrations denote final concentrations. For the addition of water vapor to the reactants, a stream of 120 mL min^{-1} dry He was bubbled through a saturator kept at a temperature of 14.7 °C. Reactant gases were subsequently added to obtain a total flow of 200 mL min^{-1}, remaining the same for all reactions.

A heating ramp of 2 °C min^{-1} from 50 °C up to 650 °C was utilized for the determination of the water-gas shift reaction. The gas mixture consists of 1% CO (Linde, Purity 4.5) and 1% H_2O. The He stream (160 mL min^{-1}) was saturated with water vapor by bubbling He through deionized and thermostatted (10.0 °C) water (Merck, ultra-pure Milli-Q 18.2 MΩ).

For CO oxidation, the temperature range was set to between 50 °C and 400 °C and the heating ramp was adjusted to 5 °C min^{-1}. As reactants 1% CO (Linde, Purity 4.5) and 0.5% O_2 (Linde, Purity 4.5) were used.

To determine the activity of NO reduction under CO excess and under the presence of O_2, a heating rate of 2 °C min^{-1} from 50 °C to 500 °C was exploited. In a more realistic gas atmosphere, the samples were exposed to a mixture of 0.25% NO, 1.25% CO, 1% H_2O with and without 0.5% O_2 (NO:CO:H_2O = 1:5:4 or NO:CO:H_2O:O_2 = 1:5:4:2). Water vapor was added in the same way as for the humid NO+CO reaction.

All reaction conditions are summarized in a table given in the SI, App. G, Table S5.

3. Results and discussion

The Results and Discussion chapter is organized as follows: at first, we structurally characterize the Cu(Pd)/LCM interface to verify the exsolution of Cu and/or alloyed Cu-Pd particles. In this respect, we combine bulk and in situ surface chemical characterization by electron microscopy and in situ XPS, respectively. In a second step, we will focus on the catalytic consequences of the formation of the metal/mixed oxide interface under more realistic de-NO_x conditions including water in comparison to the dry NO+CO model reaction. We will subsequently focus on the water-gas shift and CO oxidation behavior and in a final step discuss the consequences of excess water and CO as well as the addition of O_2.

3.1. Copper exsolution from LCM55 during the humid NO+CO reaction: bulk structural consequences

The structural and topological motifs of nanoparticular Cu and Cu_xPd_y/perovskite interfaces were analyzed by electron microscopy. To ensure the exsolution of metallic particles from the perovskite lattice and to form the desired Cu/LCM55 or Cu_xPd_y/LCM55 interface, all samples undergo an annealing step in humified NO+CO atmosphere (1% each in He) at 450 °C for 2 h. This state is from now on termed “pre-activated (P.A.) state” equal to a Cu/LCM or Cu_xPd_y/LCM interface. The state after calcination is from now on termed “as-synthesized (A.S.) state” being equal to a bare LCM55 perovskite motif or a PdO_x/LCM55 interface in case of the Pd-impregnation approach. The corresponding X-ray diffractograms of the transformation of the as-synthesized (A.S.) catalyst into the pre-activated (P.A) state are given in the SI, App. H, Fig. S5. The XRD characterization confirms the exsolution of metallic Cu/Cu_xPd_y particles after pre-activation. High-resolution imaging in combination with elemental mapping by energy dispersive X-ray imaging directly provides evidence for nanoparticular metallic Cu particles in pure LCM55, as well as Pd-alloyed Cu particles on Pd-doped LCM55 and Pd-impregnated LCM55, after a treatment in a humid NO+CO reaction mixture (Fig. 1 and SI, App. I, Figs. S6 and S7). EDX area analysis of the particles results in the quantification of the Cu and Pd content (SI, App. J, Table S6). In the case of Pd-doped LCM55, synthesized via the sol-gel route, an averaged composition of $Cu_{0.94\pm0.01}Pd_{0.06\pm0.01}$ was found. Hereafter, this particle composition is used synonymously with a "low-Pd-particle-content". In contrast, the Pd-impregnated LCM55, synthesized via the wet-impregnation approach, shows an averaged composition of $Cu_{0.62\pm0.01}Pd_{0.38\pm0.01}$ and thereby a clear enrichment of Pd due to the higher amount at the surface. From now on, this particle

Table 1
Summarizing table illustrating frequently used abbreviations and details regarding the nominal and effective composition and the particle and surface properties.

Abbreviation	Synthesis type	Catalyst state	Nominal Composition	Activation treatment	Effective Composition	Exsolved particle size by TEM / nm	surface area by BET / m^2 g^{-1}
LCM55	SG sol-gel	A.S. as-synthesized	$LaCu_{0.5}Mn_{0.5}O_{3-\delta}$	none	$LaCu_{0.5}Mn_{0.5}O_{3-\delta}$	N/A	11
		P.A. pre-activated	$LaCu_{0.5}Mn_{0.5}O_{3-\delta}$	H_2O, NO,CO 1% each in He 450 °C, 2 h	$LaCu_{0.5-x}Mn_{0.5}O_{3-\delta}$ + x Cu exsolved	~ 5–10	
LCM55 0.86 wt% Pd **SG**	SG sol-gel	A.S. as-synthesized	$La(Cu_{0.5}Mn_{0.5})_{0.98}Pd_{0.02}O_{3-\delta}$	none	$La(Cu_{0.5}Mn_{0.5})_{0.98}$ $Pd_{0.02}O_{3-\delta}$	N/A	5
		P.A. pre-activated	$La(Cu_{0.5}Mn_{0.5})_{0.98}Pd_{0.02}O_{3-\delta}$	H_2O, NO,CO 1% each in He 450 °C, 2 h	$La(Cu_{0.5-0.94x}Mn_{0.5})_{0.98}$ $Pd_{0.02-0.06x}O_{3-\delta}$ + x $Cu_{0.94\pm0.01}Pd_{0.06\pm0.01}$ "low-Pd-particle-content"	~ 5–10	
LCM55 0.86 wt% Pd **IM**	IM **im**pregnation	A.S. as-synthesized	$LaCu_{0.5}Mn_{0.5}O_{3-\delta}$ + 0,02 Pd impregnated	none	$LaCu_{0.5}Mn_{0.5}O_{3-\delta}$ + 0,02 Pd impregnated	N/A	16
		P.A. pre-activated	$LaCu_{0.5}Mn_{0.5}O_{3-\delta}$ + 0,02 Pd impregnated	H_2O, NO,CO 1% each in He 450 °C, 2 h	$La(Cu_{0.5-0.62x}Mn_{0.5})O_{3-\delta}$ + (0,02–0,38x) Pd + x $Cu_{0.62\pm0.01}Pd_{0.38\pm0.01}$ "high-Pd-particle-content"	~ 5–10	

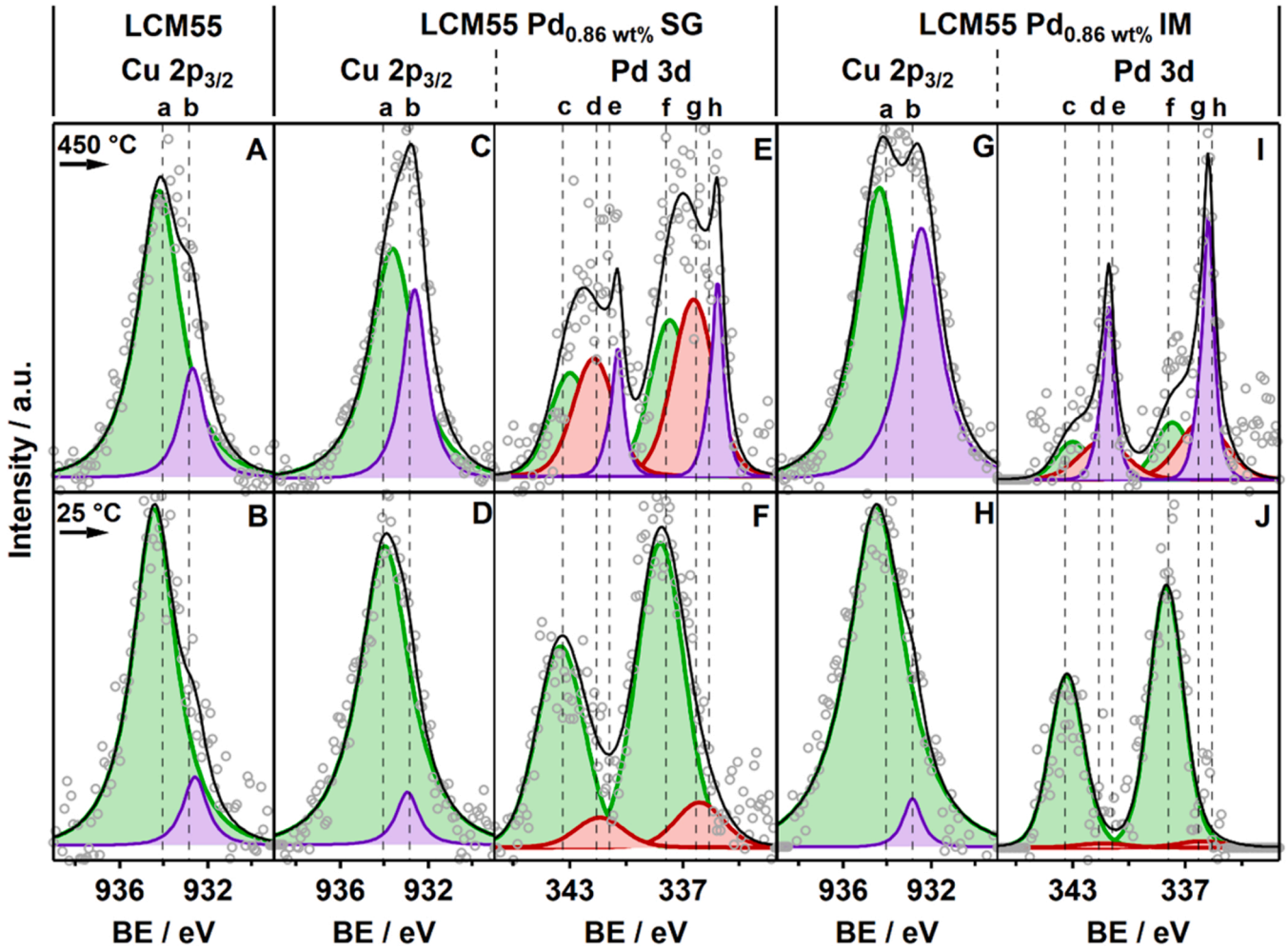

Fig. 2. XP spectra of the Pd 3d and Cu $2p_{3/2}$ region recorded in situ under CO + NO + H_2O atmosphere (0.3 mbar each) at 25 °C and 450 °C for pure LCM55, 0.86 wt % Pd-doped LCM55 via the sol-gel route and 0.86 wt% Pd-impregnated LCM55. Experimental data: grey circles; green-shaded fit components: oxidized Pd(IV) or Cu (II); red-shaded fit components: oxidized Pd(II); violet-shaded fit components: metallic or alloyed Pd(0)/Cu(0) or Cu(I). Resulting fit envelope: black line. Vertical dashed lines: BE (a-h) reference values for (a) Cu(II) $2p_{3/2}$ 934.1 eV, (b) Cu(0) $2p_{3/2}$ 932.9 eV, (SI, App. C, Fig. S1 and Table S1), (c) Pd(IV) $3d_{3/2}$ 343.3 eV, (d) Pd(II) $3d_{3/2}$ 341.6 eV, (e) Pd(0) $3d_{3/2}$ 341.2 eV, (f) Pd(IV) $3d_{5/2}$ 337.9 eV, (g) Pd(II) $3d_{5/2}$ 336.3 eV and (h) Pd(0) $3d_{5/2}$ 335.6 eV [36–39].

composition is used synonymously with a "high-Pd-particle-content". No pure Pd particles were detected after activation. Exsolution of Cu and Cu_xPd_y particles under humid NO+CO conditions show clear similarities in particle size (5–10 nm) and shape to the already reported exsolution of such entities under dry NO+CO conditions [28]. The bar graph panels provide a schematic outlook on the influence on the catalytic activity

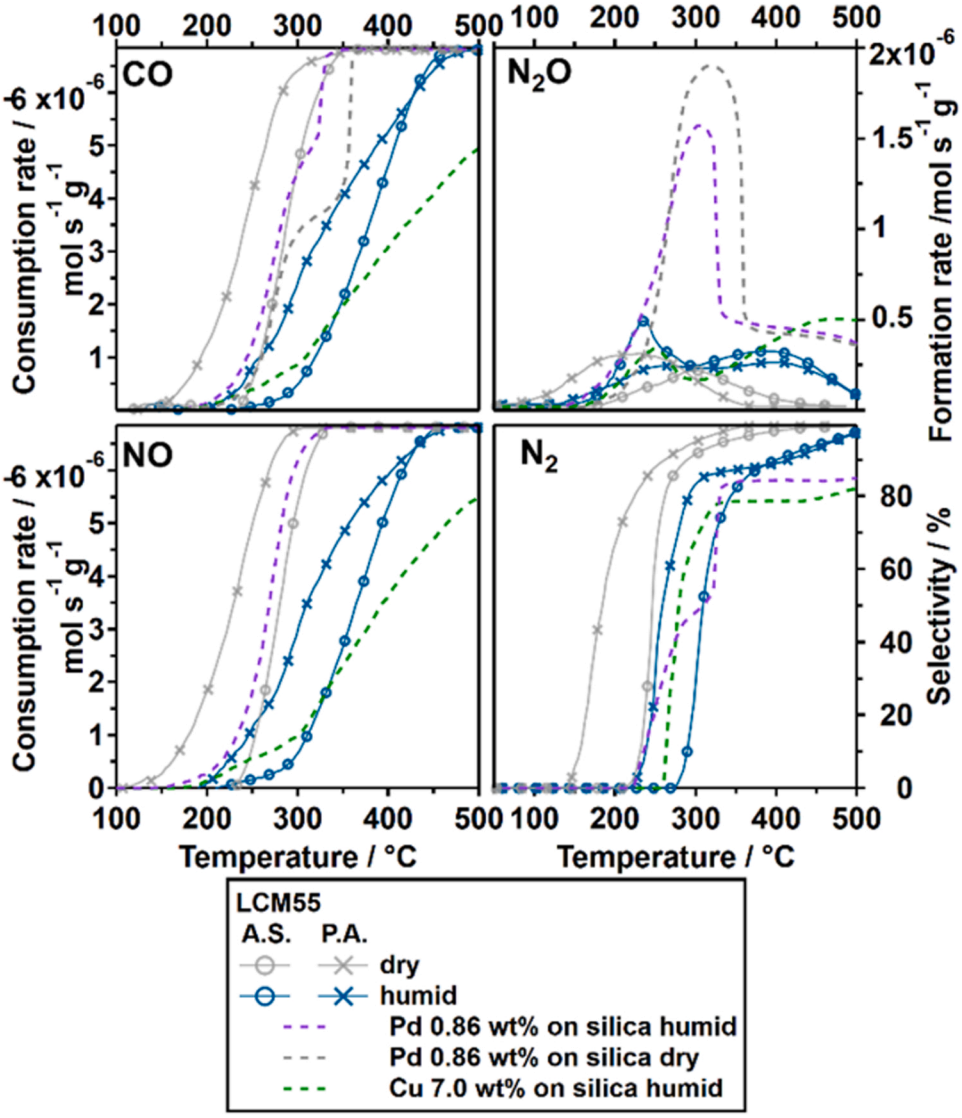

Fig. 3. Consumption rates of CO and NO, formation rate of intermediate N_2O and N_2-selectivity are shown in four separate panels. The rate profiles are plotted versus the reaction temperature for both dry and humid NO + CO reaction conditions. The performance of pure LCM55 under dry (grey trace) and humid (dark blue trace) conditions are referenced to 0.86 wt % Pd/SiO_2 (grey and violet dashed trace for dry and humid conditions, respectively) and 7.0 wt % Cu/SiO_2 (dark green dashed trace). The catalytic performance of the A.S. catalyst state is illustrated by profiles with open circles whereas crosses indicate the P.A. state of the catalyst. GHSV = $9.6{\cdot}10^3$ h^{-1}.

based on two factors (i) the addition of water vapor to the reaction mixture and (ii) the formation of metallic particles via exsolution, both in detail discussed in Section 3.3. "Reduction of NO by CO under humid conditions".

Table 1 summarizes frequently used abbreviations, terms and catalysts properties (e.g. nominal and effective composition, activation treatment, particle and surface properties).

3.2. *Surface-chemical consequences of copper exsolution from LCM55 during the humid NO+CO reaction*

To relate the bulk characterization to eventual chemical changes at the surface, in situ NAP XPS measurements were carried out during activation in humid NO+CO reaction mixtures. High-resolution scans of the Pd 3d and Cu $2p_{3/2}$ regions at selected temperatures of 25 °C and 450 °C in NO + CO + H_2O (0.3 mbar each) show clear evidence of the transformation of the synthesized Pd(IV) and Cu(II) lattice states toward exsolved Pd(0) and Cu(0) state during the annealing procedure (Fig. 2). The latter (shown in Panels A-F) support the scenario of reductive exsolution of metallic/alloyed Cu_xPd_y particles by a clear increase of the Cu(0/I) contribution (violet-shaded fit, index b) at 450 °C compared to the amount of Cu(II) (green-shaded fit, index a). Note, that inclusion of a component representing Cu(0/I) also in the fits of the respective spectra at 25 °C is necessary to describe the experimental data. This is plausible from our previous studies on LCM materials with a high Cu content. LCM55 is already at the verge of structural breakdown and even higher Cu contents inevitably lead to Cu excess and parasitic structures.[28] We, therefore, cannot exclude a minute contribution of small Cu seeds, that are invisible in both XRD and the resolution of the TEM used in this study. Remarkable is the more pronounced increase of the Cu(0/I) peak in the Pd containing catalysts, hence, Pd is facilitating the reductive particle exsolution. Residual Cu(II) species recorded in the Cu $2p_{3/2}$ region at 450 °C show the validity of an intact perovskite motif (cf. Fig. 1). The fitting procedure of the Cu $2p_{3/2}$ XP spectra is based on XP-spectra of Cu(II), Cu(I) and Cu(0) reference substances, the resulting constrains (e.g., BE, full-width-half-maximum and deviations) are summarizing in the SI, App. C in Table S1.

The oxidized Pd 3d peaks (Panels F and J, green- and red-shaded) recorded at 25 °C shifts toward a metallic-like and/or alloyed Pd state (panel E and I, violet-shaded) at 450 °C. For the Pd-doped LCM55 sol-gel sample, compared to Pd-impregnated LCM55, this behavior is less pronounced, being consistent with the microscopically shown intact perovskite motif, still containing oxidized Pd. The binding energy (BE) of 337.9 eV of the $3d_{5/2}$ peak marked with (f) in Fig. 2 is very similar to the BE found for PdO_2, thus, a Pd(IV) valence state can be formally assigned [36–38]. The $3d_{5/2}$ peak marked with (h) at BE of 335.6 eV,

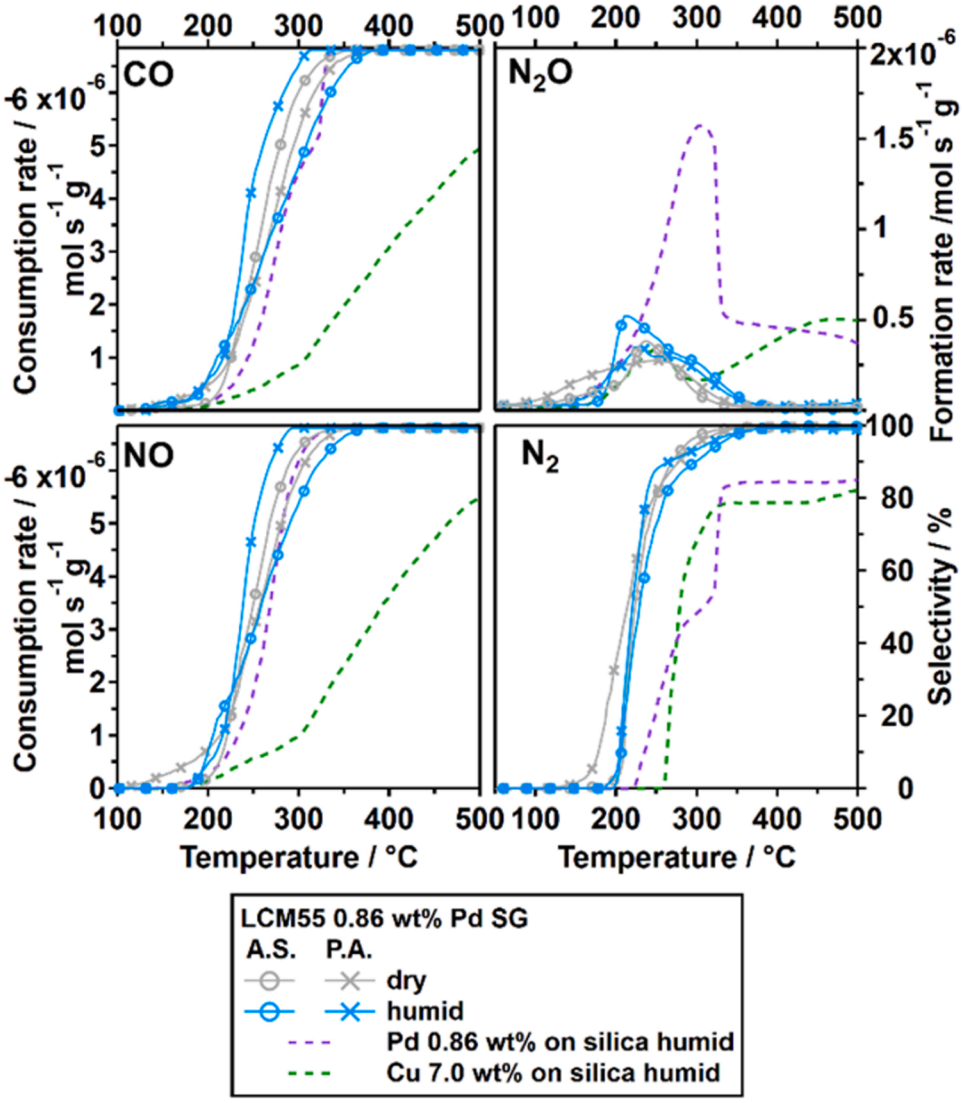

Fig. 4. Consumption rates of CO and NO, formation rate of intermediate N_2O and N_2-selectivity are shown in four separate panels. The rate profiles are plotted versus the reaction temperature for both dry and humid NO + CO reaction conditions. The performance of 0.86 wt% Pd-doped LCM55 obtained via a sol-gel route under dry (grey trace) and humid (light blue trace) conditions is referenced to 0.86 wt% Pd/SiO_2 (violet dashed trace) and 7.0 wt% Cu/SiO_2 (dark green dashed trace). The catalytic performance of the A.S. catalyst state is illustrated by traces with open circles, whereas crosses indicate the P.A. state of the catalyst. GHSV = $9.6{\cdot}10^3$ h^{-1}.

recorded at 450 °C, can be attributed to Pd(0) [38,39]. Taking into account the partial reduction of oxidized Pd species, the recorded data was fitted with a Pd(II) state (red-shaded) at a BE of 336.3 eV marked with (g) [38]. The respective peak splitting ($3d_{5/2}$ to $3d_{3/2}$) of 5.3 eV is in very good agreement with literature values for Pd, PdO and PdO_2 [36,38,39].

3.3. Reduction of NO by CO under humid conditions

One core aim of this work is to unravel the role of water participating in the reduction of NO by CO. Figs. 3–5 illustrate the catalytic behavior of pure LCM55, low-Pd-particle-content LCM55 and high-Pd-particle-content LCM55 with and without stoichiometric amounts of water vapor added to the reaction mixture (colored traces correspond to humid and grey traces to dry reaction conditions; NO:CO:(H_2O) = 1:1:(1)). A comparative approach is followed by benchmarking the performance of the LCM55-based catalysts to reference catalysts with 7.0 wt% Cu and 0.86 wt% Pd on inert silica (Cu/SiO_2 and Pd/SiO_2), indicated by dashed lines. For the LCM55-based catalysts we further distinguish between the as-synthesized (A.S.) state equal to freshly prepared catalyst, in which the Cu(Pd)/LCM55 interface is in situ evolving upon heating, and the pre-activated (P.A.) state being equal to a catalyst with an already generated metal-mixed oxide interface. These catalyst states are from now on indicated by open circles for the A.S. state and crosses for the P.A. state, respectively. More precisely, Fig. 3 highlight the consumption rate of CO and NO, the formation rate of intermediate N_2O and the selectivity toward N_2. Benefits of Cu-containing catalysts are closely tied to the ability of decomposing intermediate N_2O. Only minor amounts of N_2O are detected as compared to Pd on silica. This effective decomposition of intermediate N_2O directly leads to high N_2 selectivity.

How the catalyst state affects the catalytic performance is discussed in the following and for the sake of clarity in the context of both dry and humid reaction conditions. In particular, the performance of LCM55 improves in the onset of activity from the A.S. (bare LCM55 surface, traces with circles) to the P.A. state (Cu/LCM55 interface, traces with crosses). Cu on silica is prone to catalytically deactivate upon catalytic cycling, as proven by *ex situ* XPS characterization (SI, App. K, Figs. S8 and S9). In contrast, the Cu/LCM55 interface remains active upon additional catalytic cycles and consequently persists deactivation (SI, App. L, Fig. S10).

Comparing dry and humid conditions, a drawback of the pure LCM55 catalyst clearly is the delayed onset of catalytic activity combined with the increase in conversion temperature under humid reaction conditions. Despite this major disadvantage, the pure LCM55 catalyst is still able to achieve 100% N_2 selectivity, albeit at elevated temperatures (≈500 °C). In contrast, the reference catalysts 0.86 wt% Pd on silica and 7.0 wt% Cu on silica both saturate at 85% N_2-selectivity at 500 °C due to inefficient decomposition of intermediate N_2O. Conclusively, the

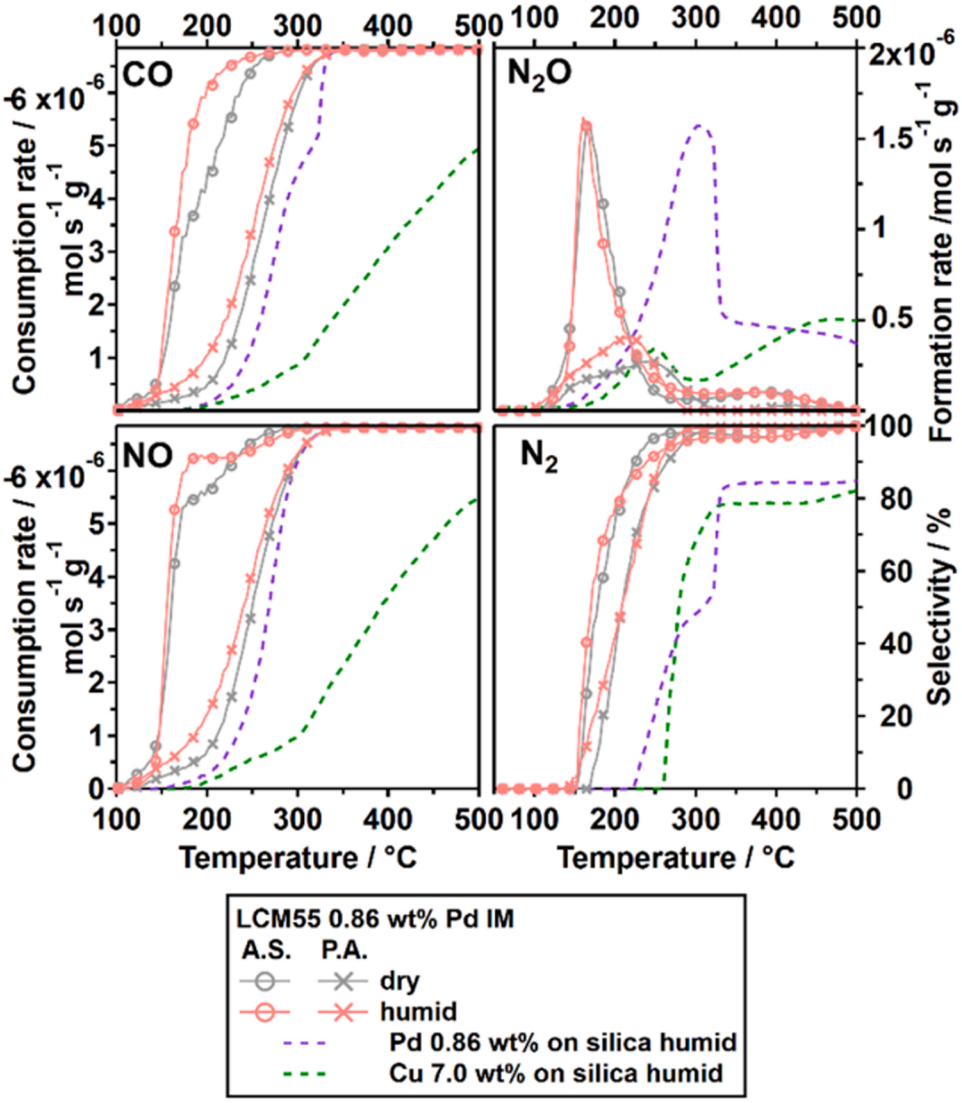

Fig. 5. Consumption rates of CO and NO, formation rate of intermediate N_2O and N_2-selectivity are shown in four separate panels. The rate profiles are plotted versus the reaction temperature for both dry and humid NO + CO reaction conditions. The performance of Pd-impregnated LCM55 with 0.86 wt% (grey and light red traces) under dry and humified conditions respectively is referenced to 0.86 wt% Pd on silica (violet dashed trace) and 7.0 wt% Cu on silica (dark green dashed trace). The catalytic performance of the A.S. catalyst state is illustrated by traces with open circles whereas crosses indicate the P.A. state of the catalyst. GHSV = $9.6{\cdot}10^3$ h^{-1}.

interfacial sites on pure LCM55 developing under in situ conditions are crucial for high N_2 selectivity.

The decrease of the CO consumption rate between ≈ 270 °C and 320 °C on the Pd reference catalyst is clearly suppressed under humid conditions compared to the more pronounced shoulder between ≈ 270 °C and 350 °C visible for dry conditions. This saturation in CO consumption corresponds to the region with a high intermediate N_2O formation rate and is most likely due to a delayed onset of reaction (2) by intermediate Pd poisoning by adsorbed CO. As thermal CO desorption from Pd under dry conditions becomes increasingly fast at around 340 °C [40], the onset of CO desorption leads to an increase of Pd surface adsorption sites for N_2O followed by a strongly accelerated N_2O decomposition above this temperature. Under humid conditions, this behavior is obviously enhanced, which is already known for Pd on inert supports [41]. The associated performance of the reference catalyst Pd on silica is illustrated in the SI, App. M, Fig. S11.

To overcome the limitations of the pure LCM55 catalyst (and, in consequence, the Cu/LCM interface forming under in situ conditions), Fig. 4 illustrates the role and benefit of the incorporation of Pd into the LCM55 catalyst on the consumption of CO and NO, as well as on the intermediate N_2O chemistry and N_2 selectivity. The profiles for the reference catalyst 0.86 wt% Pd on silica under humid conditions remain the same as in Fig. 3.

The major take-away message from Fig. 4 is that the Pd-enriched LCM55 sample with a low-Pd-particle-content exhibits a superior activity and selectivity performance with respect to pure LCM55, which apparently is not affected by the addition of stoichiometric amounts of steam. The catalytic behavior under humid conditions matches the dry conditions. We observe a weak promoting effect of water on the catalytic performance of the P.A. sample (i.e., $Cu_{0.94\pm0.01}Pd_{0.06\pm0.01}$/LCM55 interface), interpreted as a water-assisted reaction enhancement reported for Pd/perovskite interfaces, [42] similar to the Pd/Al_2O_3 study [41] in terms of adsorbate chemistry.

To study the catalytic effect of a higher Pd particle-content, Fig. 5 provides an insight into the nature of the PdO_x/LCM55 interface and how it evolves by alloying with exsolved Cu (i.e., by formation of a $Cu_{0.62\pm0.01}Pd_{0.38\pm0.01}$/LCM55 interface) and consequently, impact the overall catalytic performance. By comparing the dry and humid reaction profiles, a minor impact of water can be extracted (i.e., the light red trace is shifted to lower temperatures compared to the grey trace in Fig. 5). The promoting aspect of water vapor in the lower temperature region can be derived from the catalytic data of the reference catalyst Pd on silica (SI, App. M, Fig. S11). Fig. S11 shows a higher CO consumption rate under humid, compared to dry conditions. In agreement with the literature Pd is poisoned by dry CO in the low temperature regime, water vapor disturb the CO blocking layer by competitively absorption and enhance the CO lift-off reaction [40,41]. Via this pathway the NO adsorption is enhanced, and CO consumption rate profiles are increased

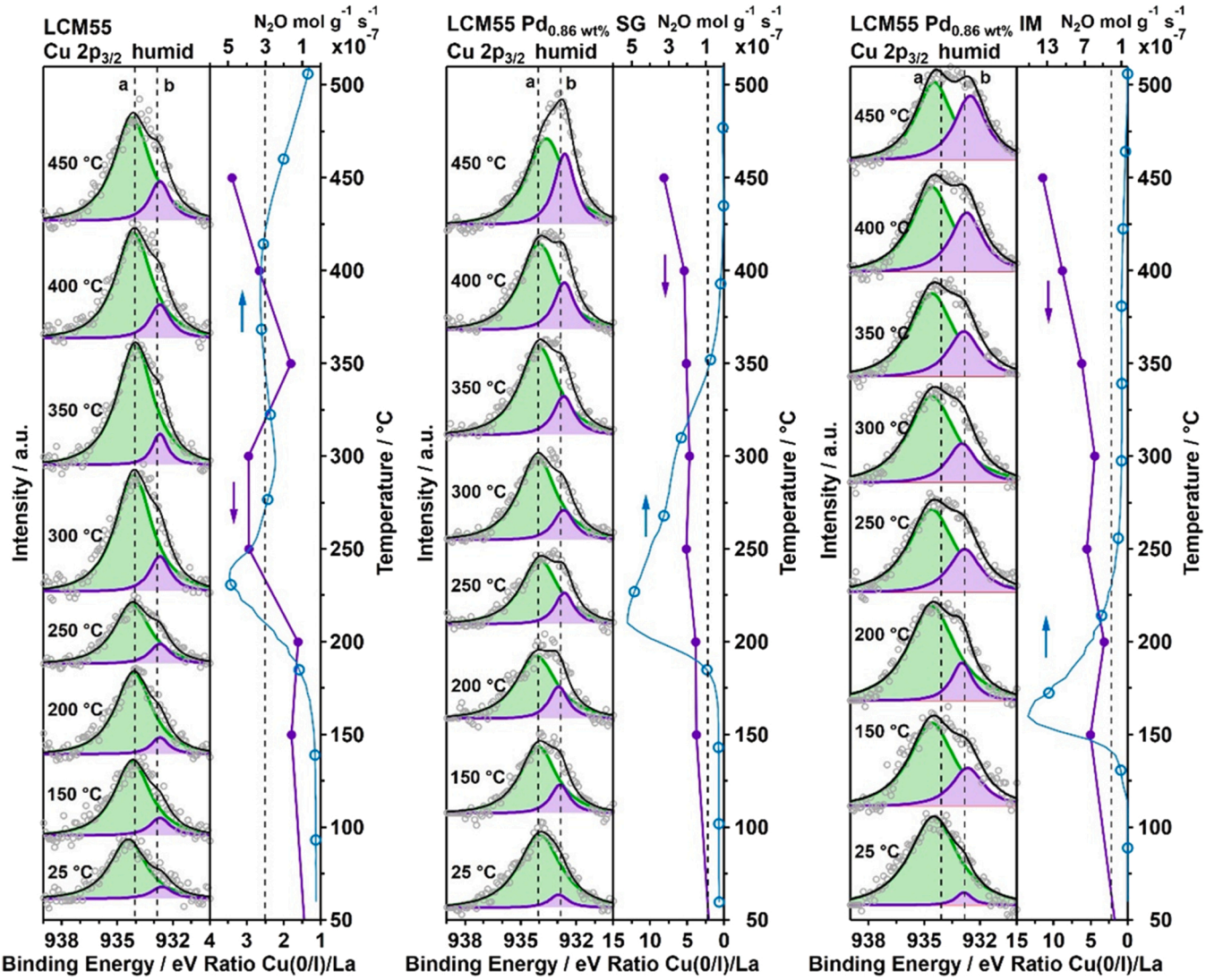

Fig. 6. Cu $2p_{3/2}$ XP spectra recorded in situ under humid CO + NO + H_2O atmosphere (0.3 mbar each) for 8 isothermal temperature steps between 25 °C and 450 °C for pure LCM55 (left panel), 0.86 wt% Pd-doped LCM55 (center panel) and Pd-impregnated LCM55 (right panel). Experimental data: gray circles; colored fits components: green shaded Cu(II) and violet shaded Cu(0/I); vertical dashed lines: BE reference values for Cu(II) 934.1 eV and Cu(0/I) 932.9 eV see SI, App. C, Fig. S1 and Table S1; fit envelope: black line. On the right side of each panel, the La $3d_{5/2}$-normalized integral intensity of Cu(0/I) (violet line with dots, determined from the color shaded peak fittings) is directly compared to the formation rate of intermediate N_2O (solid blue line with circles), as taken from the catalytic measurements.

compared to dry conditions. A similar behavior of Pd in the impregnated LCM55 sample explain the promoted catalytic performance under humid conditions.

However, the catalytic performance of the A.S. state (trace with open circles) compared to the P.A. state (trace with crosses) shows major differences in terms of CO and NO consumption, as well as N_2O formation. Starting from the A.S. state, i.e. pure Pd particles on LCM55, a highly active catalyst consumes CO and NO already below ≈ 180 °C to a large extent. The proof that the mixed-metal-oxide interface is responsible for the catalytic benefit can easily be derived by comparing the traces with those of the 0.86 wt% Pd on silica reference catalyst. In addition, the PdO_x/LCM55 interface forms intermediate N_2O at equal maximum rate ($1.5 \cdot 10^{-6}$ mol s^{-1} g^{-1}). This evidences that the partial NO reduction reaction toward N_2O is triggered by Pd and explains the pronounced NO saturation. However, less N_2O is produced at higher temperatures compared to Pd on silica, yielding a N_2 selectivity of 97% at 300 °C and 100% from 450 °C upwards. After pre-activation of the high-Pd-particle-content LCM55 catalyst ending in a final $Cu_{0.62\pm0.01}Pd_{0.38\pm0.01}$/LCM55 interface, the performance in CO and NO consumption drops to almost the same level as the low-Pd-particle-content LCM55 catalyst. This indicates the presence of structurally and/or chemically similar interfacial sites. However, the N_2O chemistry is drastically improved by pushing the N_2 selectivity toward 100% already at 280 °C, therefore showing the huge benefit of the presence of Cu.

To determine the respective activation energy (E_a) and the pre-exponential factor, kinetic studies based on the CO and NO consumption rate profiles of the LCM catalysts under humid conditions were carried out. In addition, a particle coverage estimation based on an attenuated overlayer model utilizing NAP-XPS data was established to semi-quantitatively compare reaction kinetics with active sites. In brief, the activation energy drops from pure LCM55 to Pd-impregnated LCM55 from ~65 kJ to ~57 kJ, indicating that the Cu_xPd_y/LCM55 interface lowers the activation barrier from pure Cu to CuPd alloys ($Cu_{0.94}Pd_{0.06}$ for Pd-doped LCM55 and $Cu_{0.62}Pd_{0.38}$ for Pd-impregnated LCM55). Keeping a constant pre-exponential factor is based on the assumption of comparable phase boundary dimensions on all catalysts and agrees with the estimated Cu-covered surface fraction being in a similar range for all LCM55-based catalysts. For details, we refer to the SI, App. F, Fig. S4 and Tables S3 and S4.

Based on the discussed formation and catalytic properties of different

$Cu_x(Pd_y)$/perovskite interfaces in humid NO + CO reactions and the advantages and drawbacks of exsolving Cu particles, the question now arises, how these interfaces behave under more realistic conditions and in parasitic side reactions of the de-NO_x reaction network.

3.4. Influence of copper exsolution on the N_2O chemistry

In terms of investigating how exsolved Cu affects the N_2O chemistry we monitored the chemical surface state of Cu in situ via NAP-XPS. Due to the decreased experimental pressure regime, a suppressed nucleation of Cu particle seeds and, therefore, a temperature-delayed particle growth cannot be excluded. The applied temperature and atmosphere mimic the catalytic measurements and cover both dry and humid conditions with NO + CO + (H_2O) (0.3 mbar each). For the measurements under dry conditions we refer to the SI, App. N, Fig. S12, still Fig. S12 is discussed comparatively to Fig. 6 in the following. Both Figs. 6 and S12 validate the redox state and growth of Cu in pure LCM55, 0.86 wt% Pd-doped LCM55 and 0.86 wt% Pd-impregnated LCM55 depending on the gas mixture and temperature. The recorded XP spectra are waterfall-plotted to compare effects originating from the stepwise increased temperature. In addition, Figs. 6 and S12 are matching the NAP-XPS data to the catalytically recorded N_2O formation rate.

As the La content is the same in all samples, fitting of the Cu $2p_{3/2}$ region with 2 components representing Cu(II) and Cu(0/I) and normalization of the respective integral intensities to the La $3d_{5/2}$ peak area allows to quantify both the relative and total surface-near contributions of those two distinguishable Cu oxidation states. For details concerning the normalization procedure and precise values see SI, App. O, Tables S7 and S8.

By comparing the Cu(0/I)/La ratio (violet trace) of pure LCM55 under dry and humid conditions (left panel in Fig. 6 and left panel in Fig. S12), a major increase of the ratio was detected between 150 °C and 200 °C (1.4–3.1) in the dry NO + CO mixture, followed by a growth in the Cu(0/I) contribution at higher temperatures. The evolved Cu/LCM55 interface effectively decomposes intermediate N_2O, originating from the partial reduction of NO (compare grey and dark blue N_2O-traces for dry and humid conditions respectively (Fig. 3).

The situation under humid conditions changes in a way that the major increase in the Cu(0/I)/La ratio is shifted to the temperature step between 200 °C and 250 °C. As soon as sufficiently enough Cu/LCM55 interface (e.g., more than a Cu(0/I)/La ratio of 2.5 indicated by the dashed vertical line in Fig. 6) is present, the decomposition of intermediate N_2O starts to become increasingly fast. Between 300 °C and 350 °C we observe a decrease in the Cu(0/I) contribution, interpreted as intermediate oxidation of Cu(0/I) to Cu(II) due to the presence of water in the reaction mixture. However, above 350 °C the Cu(0/I)/La ratio increases again, exceeds the critical level of 2.5 at 400 °C and directly triggers the further reduction of N_2O toward N_2. This intermediate oxidation of Cu(0/I) species under humid conditions shows a drawback of Cu and results in an overall deterioration of the catalytic activity and selectivity (c.f. Fig. 3).

By modifying the Cu/LCM55 interface toward a more noble character through alloying Cu with Pd, the water-based oxidation of the $Cu_{0.94\pm0.01}Pd_{0.06\pm0.01}$ particles can be largely suppressed (center panel in Fig. 6). Consequently, the overall activity (c.f. Fig. 4), the N_2O decomposition (Fig. 6), and therefore, the N_2-selectivity can be increased in the low-Pd-particle-content LCM55 catalyst under humid conditions. By increasing the surface availability of Pd and thus, the Pd content in the $Cu_{0.62\pm0.01}Pd_{0.38\pm0.01}$ particles (i.e., via Pd-impregnation and subsequent Cu exsolution), the stability vs. oxidative degradation can be further improved. Consequently, the visible shoulder in the N_2O trace of low-Pd-particle-content LCM55 at 300 °C (Fig. 6 center panel and Fig. 4) vanishes in the N_2O trace of high-Pd-particle-content LCM55 (Fig. 6 right panel and Fig. 5). Therefore, 100% N_2-selectivity can be achieved at ≈ 280 °C and a clear structure-reactivity relationship was established.

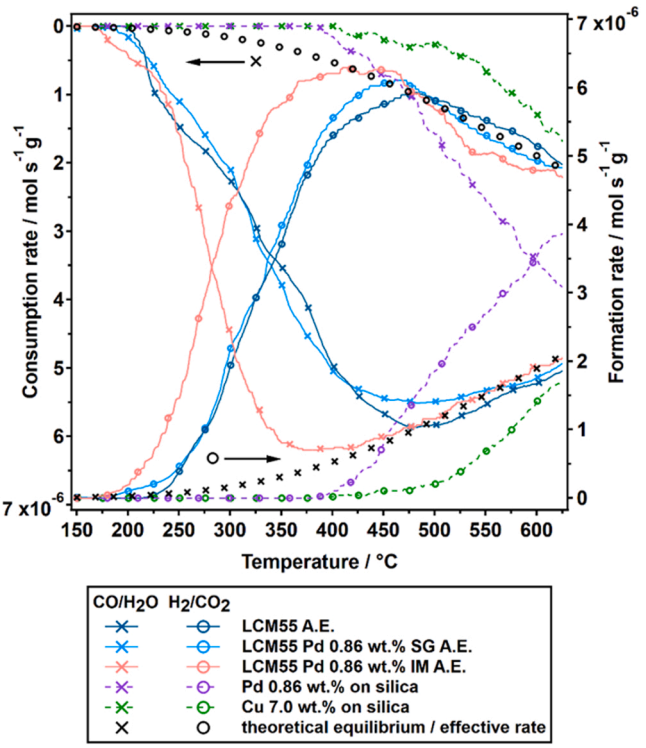

Fig. 7. Consumption rate and formation profiles of the averaged rates of CO/H_2O (crosses) and H_2/CO_2 (circles) respectively, as derived from online MS measurements. The profiles illustrate the catalytic performances of pre-activated (P.A.) states of LCM55 (dark blue), 0.86 wt% Pd-doped LCM55 (light blue), 0.86 wt% Pd-impregnated LCM55 (light red), 0.86 wt% Pd/SiO_2 (violet) and 7.0 wt% Cu/SiO_2 (green). The effective rate of the throretical equilibrium is shown with black markers. GHSV = $9.6{\cdot}10^3$ h^{-1}.

In terms of oxygen vacancies, EDX analysis (SI, App. I, Fig. S6) shows that the amount of Cu(II) in the perovskite lattice is decreased in the near region of the exsolved particle, but still remaining Cu(II) is present in this region, which allows to anticipate a certain vacancy concentration. This argumentation is supported by the catalytic data of the reference Cu on silica compared to LCM55 in the pre-activated state (Fig. 3). Both catalysts exhibit a Cu/support interface, but they differ in the oxygen vacancy concentration of the support. For this reason, the LCM55 catalyst show higher consumption rates from 200 °C onward. Both light-off curves show no significant consumption of CO or NO up to 200 °C, a possible explanation for this behavior can be extracted from the in situ NAP XPS data (Fig. 6), indicating an oxidized and consequently inactive Cu(II) state up to 200 °C. A possible oxygen-vacancy-quenching of water vapor up to 500 °C is expected to be neglectable as highly oxidizing agents (e.g. ozone) are needed to facilitate this pathway [43].

3.5. Water-gas shift activity

CO and H_2O in excess stoichiometry are the main contributors in more applied exhaust gas mixtures. To understand catalytic effects originating from the direct reaction of those [44], the water-gas shift activity was accordingly investigated (Fig. 7). As the educts (CO and H_2O) and products (CO_2 and H_2) show the same conversion trend, the respective signals were combined and averaged. As soon as a sufficient temperature is reached, the mixture (1% CO and 1% H_2O in He) approaches the theoretical WGS equilibrium profile, indicated with black markers in Fig. 7. From thermodynamics, equal contributions of CO_2/H_2 and CO/H_2O are expected at 815 °C [20]. The data obtained on the reference catalyst Cu on inert silica (green traces) agree with the

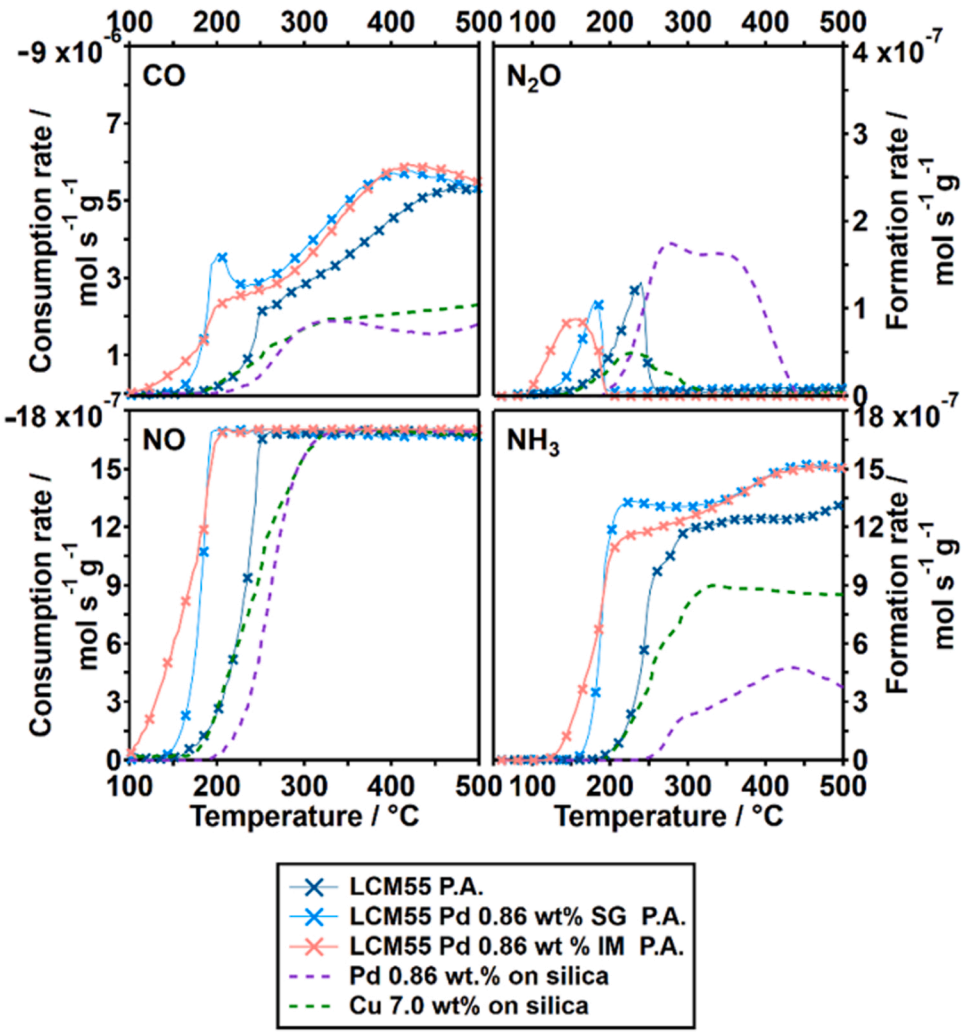

Fig. 8. Consumption rate profiles of CO and NO and the formation rates of N_2O and NH_3 as a function of reaction temperature in both CO and H_2O excess. In this experiment the ratio of NO: CO: H_2O was adjusted to 1: 5: 4. The performance of pure LCM55 (dark blue trace), of Pd-doped LCM55 (light blue trace) and of Pd-impregnated LCM55 (light red trace) the later both with 0.86 wt% Pd and all of them in the pre-activated (P.A.) state are referenced to 0.86 wt% Pd/SiO_2 (violet dashed trace) and 7.0 wt% Cu/SiO_2 (green dashed trace). GHSV = $9.6{\cdot}10^3$ h^{-1}.

reported observation of weak activity of wet-impregnated Cu/SiO_2 catalysts with comparably low Cu-loadings [45].

By comparing the trend of Cu/SiO_2 with the ones of the LCM55-based catalysts the lower onset of the conversion temperature by introducing an oxygen-deficient perovskite is remarkable. In addition, the traces of all LCM55-based catalysts differ from those of the Pd/SiO_2 by ≈ 200 °C. The further addition of Pd to LCM55 (low-Pd-particle-content, light blue trace) did not have any effect on the catalytic activity, whereas if the perovskite has a higher-Pd-particle-content, the activity is further enhanced. This indicates that the enrichment of nanoparticular Cu by alloying with more surface-abundant Pd (i.e., via impregnation) is beneficial for the overall catalyst performance. Consequently, the M/LCM55 interface (M = Cu or $Cu_{0.94\pm0.01}Pd_{0.06\pm0.01}$) shows notable WGS activity at ≈ 250 °C according to the formation of CO_2 and H_2, whereas the $Cu_{0.62\pm0.01}Pd_{0.38\pm0.01}$/LCM55 interface starts to form products already at ≈ 200 °C.

3.6. *Effect of the excess of water vapor and CO*

To investigate how CO and H_2O vapor excess affect the consumption of NO and to prove the role of H_2 evolving via the WGS route, we performed a catalytic experiment in excess CO and H_2O (0.25% NO, 1.25% CO and 1% H_2O in He (NO:CO:H_2O = 1:5:4)). Fig. 8 shows the catalytic results in terms of educt and product progress of the LCM55-based pre-activated (P.A.) catalysts with and without Pd addition. By comparing the LCM55-based catalysts we point out that, at first NO is fully consumed by CO with an increase in onset-temperature, but the reduction of NO covers the full range of nitrogen oxidation states down to NH_3. This indicates the participation of activated water to the overall reduction reaction. Before NH_3 evolves to a major extent (formation rate saturation between $12{\cdot}10^{-7}$ mol s^{-1} g^{-1} and $14{\cdot}10^{-7}$ mol s^{-1} g^{-1}), a minor amount of N_2O is formed (formation rate of ≈$1{\cdot}10^{-7}$ mol s^{-1} g^{-1}). As the NH_3 formation rate does not fully cover the consumption rate of NO, we assume a minor contribution of N_2. The behavior of Cu/SiO_2 is similar to that of LCM55, although the consumption of NO and CO is slightly delayed in temperature and the NH_3 formation remained at a formation rate of ≈ $9{\cdot}10^{-7}$ mol s^{-1} g^{-1}. This indicates that Cu is responsible for the main activity and the interface to LCM55 enhances the performance to some extent. Pd-addition to LCM55 further increases the activity at lower temperatures. Pd on silica shows an intermediate full consumption of NO toward N_2O. However, the formation rate of NH_3 is the lowest of all investigated catalysts, indicating that Pd on silica has in comparison the lowest water activation capability. The excess of CO and H_2O decreases the NO onset temperature of all LCM55-based catalysts by ≈ 50 °C, most prominently for pure LCM55. In consequence, a higher CO partial pressure increases the gas-phase reduction potential, causing an effective metal-mixed-oxide surface regeneration route by reaction of O_{ads} species (e.g., from NO dissociation) with CO. Low-temperature water-activation, however, results in a surface availability of H_{ads} coherent with the low-temperature formation of NH_3. With respect to the CO rate profiles, all LCM55-based catalysts follow more or less the theoretical WGS pathway at higher temperatures.

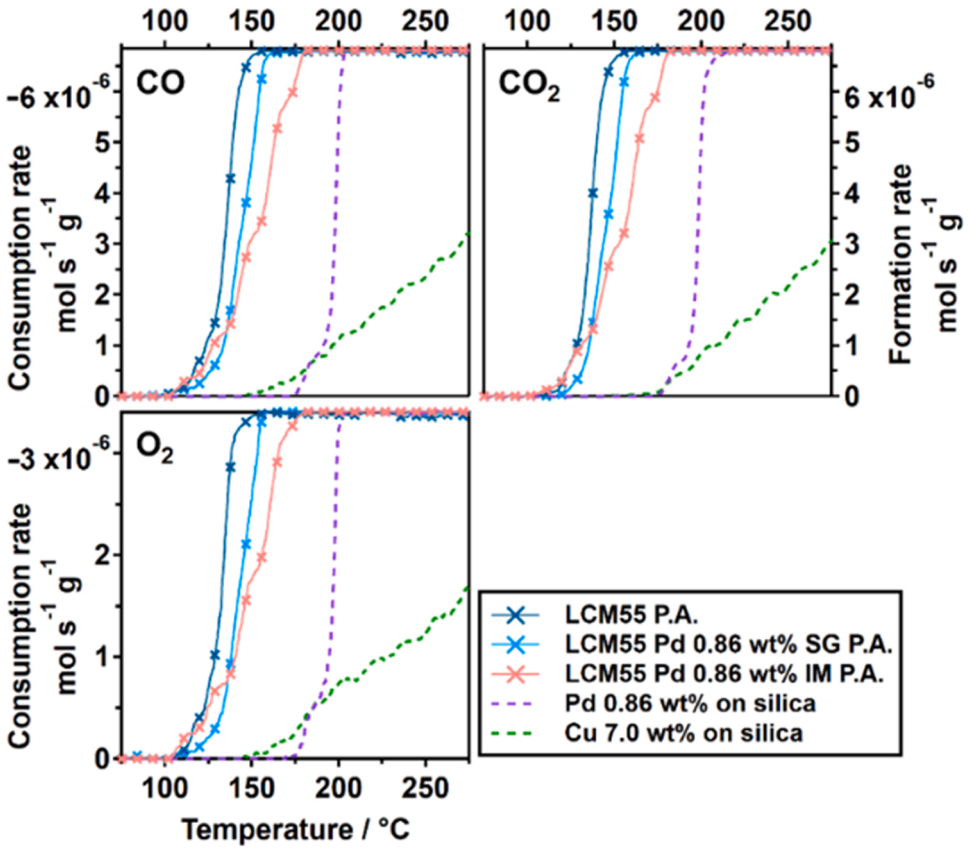

Fig. 9. Consumption rate and formation rate profiles of CO, O_2 and CO_2 respectively. The profiles illustrate the catalytic performances of LCM55 (dark blue trace), Pd-doped LCM55 (light blue trace), Pd-impregnated LCM55 (light red trace), 0.86 wt% Pd/SiO_2 (violet dashed trace) and 7.0 wt% Cu/SiO_2 (green dashed trace). GHSV = $9.6{\cdot}10^3$ h^{-1}.

3.7. CO oxidation activity

To test if the LCM55-based catalysts in their pre-activated state trigger a low-temperature CO oxidation reaction prior to a notable WGS reaction, we performed catalytic experiments in a CO + O_2 reaction mixture (Fig. 9). As Cu/SiO_2 is suffering from oxidative deactivation, a weak performance was expected [46]. Instead, the Pd/SiO_2 catalyst shows an onset at ≈ 175 °C consistent with literature [47]. We observe a low-temperature consumption of CO and O_2 on all LCM55 catalysts, which we assign to the beneficial effect of the mixed-metal oxide interface in the P.A. state. As all catalytic measurements were performed under the same catalyst quantity and GHSV, full conversion temperatures can be compared to each other. The temperature of 100% consumption of the CO:O_2 mixture 2:1 (1% CO and 0.5% O_2 in He) was detected between 150–175 °C and therefore, at 25 °C lower than the onset of the WGS reaction at least with respect to the high-Pd-particle-content LCM55 catalyst. A decrease in the temperature of full conversion from pure LCM55 (dark blue trace, Cu/LCM55 interface) over low-Pd-particle-content LCM55 (light blue trace, $Cu_{0.94\pm0.01}Pd_{0.06\pm0.01}$/LCM55 interface) toward high-Pd-particle-content LCM55 (light red trace, $Cu_{0.62\pm0.01}Pd_{0.38\pm0.01}$/LCM55 interface) was detected. This behavior can be interpreted as a shift towards the behavior of pure Pd particles suffering from increased CO poisoning in the studied temperature regime.

3.8. Effect of the addition of O_2 to reach quantitative N_2 selectivity

As the LCM55 catalysts trigger the oxidation of CO at lower temperatures than the WGS reaction, we aim on a proof combining applied de-NOx reaction conditions (excess of CO and steam) with the addition of O_2 to reach quantitative N_2 selectivity (Fig. 10). Catalytic experiments were performed using a mixture of NO: CO: H_2O: O_2 = 1: 5: 4: 2. Assuming that one CO molecule reacts with NO, the amount of O_2 added corresponds to the half-equimolar amount of CO. This approach should clarify, whether the catalysts can selectively form N_2 and CO_2 under more realistic conditions, i.e., if NO fully reacts with CO (Reaction 1) and the excess CO reacts either via the WGS pathway (Reaction 3) or is oxidized by O_2 toward CO_2 (Reaction 4).

In particular, neither NH_3, being a strong indicator for the WGS route (cf. Fig. 8), nor NO_2, originating form NO oxidation was detected, indicating high N_2 selectivity. In terms of the CO consumption rate profiles, the general catalyst performance (except Cu/SiO_2) can be interpreted as CO oxidation reaction followed by the reduction of NO by CO. Validation for this interpretation is given by the match of the NO onset temperature with the visible kink in the CO traces. In addition, the proportions of CO, NO and O_2 in the mixture illustrated by the consumption rates of CO and NO corroborate this argumentation. By increasing the temperature, firstly ≈ $60{\cdot}10^{-7}$ mol s^{-1} g^{-1} of CO were consumed by O_2 (no change in the water level was detected during the experiment), followed by a consumption of ≈ $17{\cdot}10^{-7}$ mol s^{-1} g^{-1} of CO (equimolar to NO) and, therefore, full CO conversion. However, the CO oxidation reaction on Pd-doped 0.86 wt% LCM55 and pure LCM55 (light and dark blue traces respectively) are delayed by ≈ 70 °C to ≈ 120 °C in temperature compared to Fig. 9. This decrease in activity under more oxidizing conditions implies a structural change of the reactive interface upon oxidation. This is supported by experiments on the more oxidation-stable Pd/SiO_2 (violet dashed trace) and high-Pd-particle-content LCM55 (light red trace, $Cu_{0.62\pm0.01}Pd_{0.38\pm0.01}$/LCM55 interface) catalysts, as they do not show any shift in the CO oxidation temperature. By comparing the traces of pure LCM55 with Cu/SiO_2 (green dashed trace), the influence of the interface is evident.

The NO consumption rate of pure LCM55 (dark blue trace) shows a

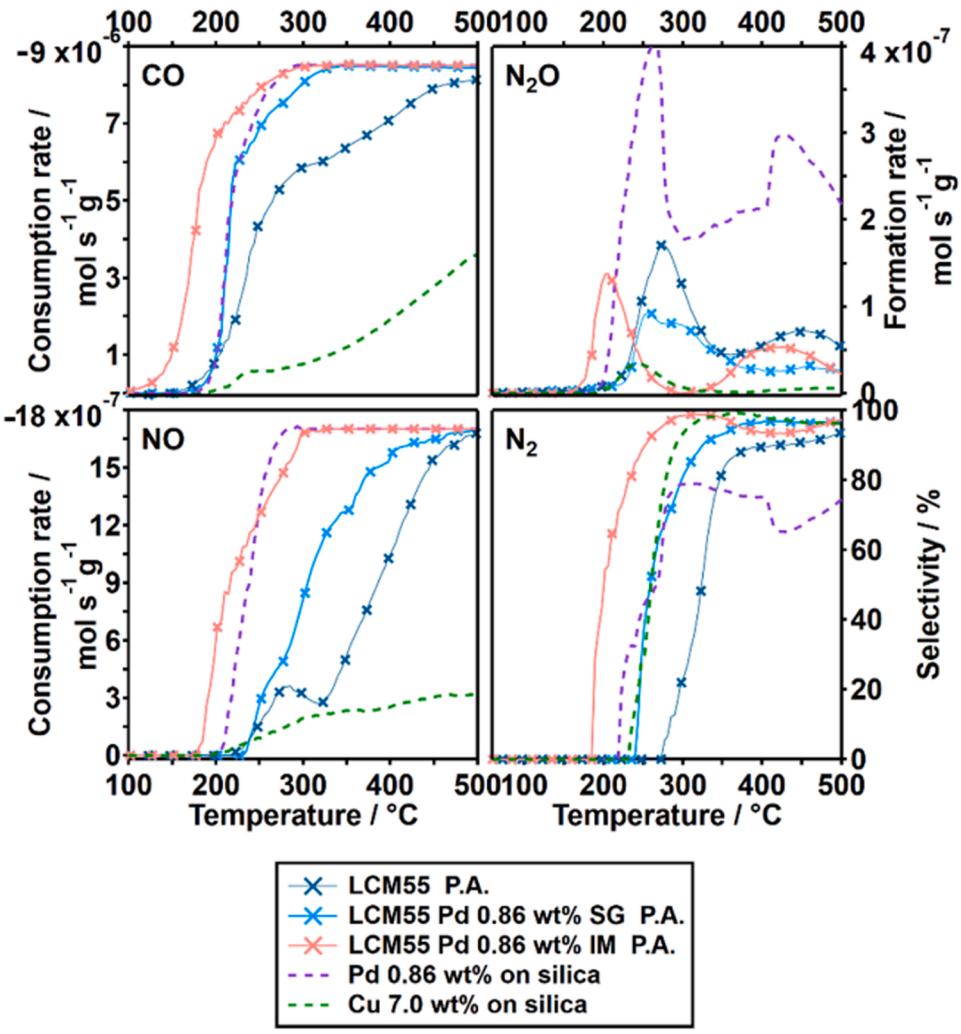

Fig. 10. Consumption rates of CO and NO, formation rate of N_2O and the N_2-selectivity as a function of temperature in a more applied reaction mixture containing NO: CO: H_2O: O_2 with a ratio of 1: 5: 4: 2. The performance of pure LCM55 (dark blue trace), of Pd-doped LCM55 (light blue trace) and of Pd-impregnated LCM55 (light red trace) the later both with 0.86 wt% Pd and all of them in the pre-activated state are compared to reference catalysts 0.86 wt% Pd on silica (violet dashed trace) and 7.0 wt% Cu on silica (green dashed trace). GHSV = $9.6{\cdot}10^3$ h^{-1}.

separation of the partial reduction of NO (Reaction 2) from the reduction toward N_2 (Reaction 1). The first peak at ≈ 280 °C directly corresponds to full conversion of NO into N_2O (i.e., Reaction 2, conversion of $\approx 3{\cdot}10^{-7}$ mol s^{-1} g^{-1} of NO into $\approx 1.5{\cdot}10^{-7}$ mol s^{-1} g^{-1} of N_2O). Although this behavior is not visible in the low-Pd-particle-content LCM55 NO consumption rate profile (light blue), the N_2O formation onset (≈280 °C) is consistent with pure LCM55. In contrast, the onset temperature of N_2O evolution of the high-Pd-particle-content LCM55 is shifted by ≈ 100 °C to lower temperatures (180 °C) and resembles that of Pd/SiO_2 (200 °C). In addition, the N_2O formation rate of the Cu-containing LCM-based catalysts is much less compared to the Pd on silica reference, implying a direct consequence of surface abundant Cu. The $Cu_{0.62\pm0.01}Pd_{0.38\pm0.01}$/LCM55 interface (light red trace) combines these two aspects by subsequently triggering 100% N_2-selectivity below 300 °C. How this optimum point in activity and selectivity of Pd-impregnated LCM55 catalysts evolve over time was further proven by a long-term durability test for 72 h (see SI, App. P, Fig. S13). No loss in activity was observed under the isothermal conditions at 295 °C for 72 h.

4. Conclusions

As a bifunctionally operating catalyst surface/interface acting on each reaction of the de-NO_x reaction network essentially contributes to obtain high activity and selectivity, we have discussed the advantages and drawbacks of exploiting Cu in realistic de-NO_x reaction mixtures. Both the advantages and drawbacks of Cu are strongly connected to its surface state, which is consequently affected by the applied reaction conditions.

In contrast to dry conditions, where metallic Cu is prone to decompose N_2O effectively below 350 °C (enhancing the N_2-selectivity), the Cu surface remains mainly oxidized under humid conditions, shifting the N_2O decomposition to a higher temperature regime above 500 °C, thereby decreasing the N_2 selectivity (c.f. Fig. 3). By alloying with more noble elements like Pd, the surface state of Cu can be prevented from oxidation even in the presence of water or oxygen, retaining the N_2O chemistry related to the presence of metalic Cu.

In essence, the catalytic behavior in the WGS reaction, CO oxidation and NO reduction reaction under the studied humid conditions is essentially independent of the Pd content. However, under highly oxidizing conditions in the presence of O_2, only the Pd-enriched $Cu_{0.62\pm0.01}Pd_{0.38\pm0.01}$/LCM55 interface unfolds its beneficial stability and N_2O chemistry.

This indicates that the oxidation-prone character of Cu can be compensated by alloying with metals with a relatively more noble character. Most importantly, the adjusted Cu_xPd_y composition only shows its beneficial performance in contact to an appropriate oxygen deficient perovskite, in combination yielding a strong competitor to commercial oxide-supported catalysts. We have shown how the combined concept of impregnation with a noble metal and exsolution of Cu yields a reactive $Cu_x(Pd_y)$/perovskite interface, which allows to overcome the discussed limitations of Cu under realistic de-NO_x conditions.

The proof-of-principle provides a first step towards the economization of noble metals by careful adjustment of the noble metal content at the surface in future works.

Supporting Information

Synthesis of reference catalysts. NAP XPS experimental setup. XP and Auger spectra of Cu reference substances (metallic Cu, Cu_2O and CuO) and reference-based data evaluation procedure of the in situ XP and Auger spectra of the Cu 2p3/2 and Cu LMM region. Data evaluation of the catalytic tests. BET specific surface area measurements of undoped and Pd-doped LCM-based catalysts and reference catalysts. Kinetic studies and particle coverage estimation of LCM-based catalysts. Reaction conditions. XRD characterization of the LCM-based catalysts. Microscopic verification of Cu and CuPd exsolution on LCM55-based catalysts EDXS analysis. Particle composition characterization of LCM55-based catalysts by TEM and EDXS area analysis – summarized results. XPS investigation and deactivation via catalytic cycling of the Cu/SiO_2 reference catalyst. Catalytic characterization of LCM55 upon cycling. Catalytic performance of the Pd/SiO_2 reference catalyst under dry and humid deNOx conditions. In situ NAP XPS measurements of LCM55 based catalysts under dry conditions. XPS normalization of the Cu $2p_{3/2}$ intensity to La $3d_{5/2}$. Long-term durability measurement of high-Pd-particle-content LCM55.

CRediT authorship contribution statement

Christoph W. Thurner: (lead) Sample preparation, Catalytic tests, XRD and NAP-XPS experiments, Data analyzation and evaluation, Writing – original draft. **Xaver Drexler**: (supporting) Sample preparation, Catalytic tests, Data analyzation and evaluation, XRD experiments, Mid-term durability measurements. **Lander Haug**: (supporting) Contribution in NAP-XPS investigations. **Daniel Winkler**: (supporting) Contributing in XPS investigations, Support in XP data analyzation. **Julia Kunze-Liebhäuser**: (supporting) Administration concerning the XPS investigations. **Johannes Bernardi**: (supporting) TEM investigation after sample synthesis. **Bernhard Klötzer**: (supporting) Project administration, Support in writing of original draft, Validation. **Simon Penner**: (corresponding) Project administration, Support in writing of original draft, Validation.

Declaration of Competing Interest

The authors declare that they have no known competing financial interests or personal relationships that could have appeared to influence the work reported in this paper.

Data availability

Data will be made available on request.

Acknowledgements

Financial support was provided by the framework of the platform Materials- and Nanoscience and the special PhD program “Reactivity and Catalysis” at the University of Innsbruck. We particularly thank the group of H. Huppertz from the Department of General, Inorganic and Theoretical Chemistry of the University of Innsbruck for providing the possibility of using their X-ray diffractometer for *ex situ* powder XRD measurements. J.K.-L. acknowledges funding by the Austrian Science Fund (FWF) via grant I-4114-N37. The Austrian Promotion Agency (FFG) is acknowledged for funding of the near ambient pressure XPS instrument through F&E infrastructure project 870523 “XPS In-situ and Operando Investigations of Functional Materials”. Additionally, L. Haug acknowledges funding through FFG project 870523, and D. Winkler is a recipient of a DOC Fellowship of the Austrian Academy of Sciences at the Department of Physical Chemistry.

Appendix A. Supporting information

Supplementary data associated with this article can be found in the online version at doi:10.1016/j.apcatb.2023.122693.

References

[1] T.F. Stocker, D. Qin, G.-K. Plattner, M. Tignor, S.K. Allen, J. Boschung, A. Nauels, Y. Xia, V. Bex, P.M. Midgley (Eds.), IPCC: Climate Change: The Physical Science Basis. Contribution of Working Group I to the Fifth Assessment Report of the Intergovernmental Panel on Climate Change, Cambridge University Press, Cambridge, United Kingdom and New York, NY, USA, 2013, p. 1535.
[2] J. Perez-Ramirez, F. Kapteijn, K. Schoffel, J.A. Moulijn, Formation and control of N_2O in nitric acid production - Where do we stand today? Appl. Catal. B 44 (2003) 117–151.
[3] M.H. Thiemens, W.C. Trogler, Nylon production - an unknown source of atmospheric nitrous-oxide, Science 251 (1991) 932–934.
[4] E.C. Adams, M. Skoglundh, M. Folic, E.C. Bendixen, P. Gabrielsson, P.A. Carlsson, Ammonia formation over supported platinum and palladium catalysts, Appl. Catal. B 165 (2015) 10–19.
[5] E.C. Adams, M. Skoglundh, P. Gabrielsson, M. Laurell, P.A. Carlsson, Ammonia formation over Pd/Al_2O_3 modified with cerium and barium, Catal. Today 267 (2016) 210–216.
[6] P.R. Dasari, R. Muncrief, M.P. Harold, Elucidating NH_3 formation during NO_x reduction by CO on $Pt–BaO/Al_2O_3$ in excess water, Catal. Today 184 (2012) 43–53.
[7] S. Roy, M.S. Hegde, G. Madras, Catalysis for NOx abatement, Appl. Energy 86 (2009) 2283–2297.
[8] M. Pena, J. Fierro, Chemical structures and performance of perovskite oxides, Chem. Rev. 101 (2001) 1981–2018.
[9] D.B. Meadowcroft, Low-cost oxygen electrode material, Nature 226 (1970) 847–848.
[10] W.F. Libby, Promising catalyst for auto exhaust, Science 171 (1971) 499–500.
[11] H. Kim Chang, G. Qi, K. Dahlberg, W. Li, Strontium-doped perovskites rival platinum catalysts for treating NO_x in simulated diesel exhaust, Science 327 (2010) 1624–1627.
[12] R.J.H. Voorhoeve, D.W. Johnson, J.P. Remeika, P.K. Gallagher, Perovskite oxides: materials science in catalysis, Science 195 (1977) 827–833.
[13] Y. Nishihata, J. Mizuki, T. Akao, H. Tanaka, M. Uenishi, M. Kimura, T. Okamoto, N. Hamada, Self-regeneration of a Pd-perovskite catalyst for automotive emissions control, Nature 418 (2002) 164–167.
[14] Y. Nishihata, J. Mizuki, H. Tanaka, M. Uenishi, M. Kimura, Self-regeneration of palladium-perovskite catalysts in modem automobiles, J. Phys. Chem. Solids 66 (2005) 274–282.
[15] H. Tanaka, I. Tan, M. Uenishi, M. Taniguchi, M. Kimura, Y. Nishihata, J. Mizuki, $LaFePdO_3$ perovskite automotive catalyst having a self-regenerative function, J. Alloy. Compd. 408 (2006) 1071–1077.
[16] M.B. Katz, G.W. Graham, Y.W. Duan, H. Liu, C. Adamo, D.G. Schlom, X.Q. Pan, Self-regeneration of Pd-$LaFeO_3$ catalysts: new insight from atomic-resolution electron microscopy, J. Am. Chem. Soc. 133 (2011) 18090–18093.
[17] J.H. Chen, M.Q. Shen, X.Q. Wang, G.S. Qi, J. Wang, W. Li, The influence of nonstoichiometry on $LaMnO_3$ perovskite for catalytic NO oxidation, Appl. Catal. B 134 (2013) 251–257.
[18] J.W. Evans, M.S. Wainwright, A.J. Bridgewater, D.J. Young, On the determination of copper surface-area by reaction with nitrous-oxide, Appl. Catal. 7 (1983) 75–83.
[19] J.J. Scholten, J.A. Konvalinks, Reaction of nitrous oxide with copper surfaces - application to determination of free-copper surface areas, J. Chem. Soc. Faraday Trans. 65 (1969) 2465.
[20] D.C. Grenoble, M.M. Estadt, D.F. Ollis, The chemistry and catalysis of the water gas shift reaction: 1. The kinetics over supported metal catalysts, J. Catal. 67 (1981) 90–102.
[21] A. Tarjomannejad, A. Niaei, A. Farzi, D. Salari, P.R. Zonouz, Catalytic Oxidation of CO Over $LaMn_{1-x}B_xO_3$ (B = Cu, Fe) Perovskite-type Oxides, Catal. Lett. 146 (2016) 1544–1551.
[22] H. Tanaka, M. Taniguchi, M. Uenishi, N. Kajita, I. Tan, Y. Nishihata, J. Mizuki, K. Narita, M. Kimura, K. Kaneko, Self-regenerating Rh- and Pt-based perovskite catalysts for automotive-emissions control, Angew. Chem. Int. Ed. 45 (2006) 5998–6002.
[23] S. Dai, S.Y. Zhang, M.B. Katz, G.W. Graham, X.Q. Pan, In Situ Observation of Rh-$CaTiO_3$ Catalysts during Reduction and Oxidation Treatments by Transmission Electron Microscopy, ACS Catal. 7 (2017) 1579–1582.
[24] M.B. Katz, S.Y. Zhang, Y.W. Duan, H.J. Wang, M.H. Fang, K. Zhang, B.H. Li, G. W. Graham, X.Q. Pan, Reversible precipitation/dissolution of precious-metal clusters in perovskite-based catalyst materials: Bulk versus surface re-dispersion, J. Catal. 293 (2012) 145–148.
[25] S.Y. Zhang, M.B. Katz, S. Dai, K. Zhang, X.F. Du, G.W. Graham, X.Q. Pan, New Atomic-Scale Insight into Self-Regeneration of Pt-$CaTiO_3$ Catalysts: Incipient Redox-Induced Structures Revealed by a Small-Angle Tilting STEM Technique, J. Phys. Chem. C. 121 (2017) 17348–17353.
[26] D. Neagu, V. Kyriakou, I.L. Roiban, M. Aouine, C.Y. Tang, A. Caravaca, K. Kousi, I. Schreur-Piet, I.S. Metcalfe, P. Vernoux, M.C.M. van de Sanden, M.N. Tsampas, In situ observation of nanoparticle exsolution from perovskite oxides: from atomic

scale mechanistic insight to nanostructure tailoring, Acs Nano 13 (2019) 12996–13005.
[27] A. Mohammadi, A. Farzi, C. Thurner, B. Kloetzer, S. Schwarz, J. Bernardi, A. Niaei, S. Penner, Tailoring the metal-perovskite interface for promotional steering of the catalytic NO reduction by CO in the presence of H_2O on Pd-lanthanum iron manganite composites, Appl. Catal. B 307 (2022).
[28] C.W. Thurner, N. Bonmassar, D. Winkler, L. Haug, K. Ploner, P. Delir Kheyrollahi Nezhad, X. Drexler, A. Mohammadi, P.A. van Aken, J. Kunze-Liebhäuser, A. Niaei, J. Bernardi, B. Klötzer, S. Penner, Who Does the Job? How Copper Can Replace Noble Metals in Sustainable Catalysis by the Formation of Copper–Mixed Oxide Interfaces, ACS Catal. 12 (2022) 7696–7708.
[29] E. Campagnoli, A. Tavares, L. Fabbrini, I. Rossetti, Y.A. Dubitsky, A. Zaopo, L. Forni, Effect of preparation method on activity and stability of $LaMnO_3$ and LaCoO3 catalysts for the flameless combustion of methane, Appl. Catal. B 55 (2005) 133–139.
[30] A. Glisenti, M. Pacella, M. Guiotto, M.M. Natile, P. Canu, Largely Cu-doped $LaCo_{1-x}Cu_xO_3$ perovskites for TWC: Toward new PGM-free catalysts, Appl. Catal. B 180 (2016) 94–105.
[31] A.N. Petrov, A.Y. Zuev, I.L. Tikchonova, V.I. Voronin, Crystal and defect structure of the mixed oxides $LaMn_{1-z}Cu_zO_{3\ +/-\ y}$ ($0 <= z <= 0.4$), Solid State Ion. 129 (2000) 179–188.
[32] S. Yanagisawa, A. Uozumi, I. Hamada, Y. Morikawa, Search for a Self-Regenerating Perovskite Catalyst Using ab Initio Thermodynamics Calculations, J. Phys. Chem. C. 117 (2013) 1278–1286.
[33] P.F. Cao, P.Y. Tang, M.F. Bekheet, H.C. Du, L.Y. Yang, L. Haug, A. Gili, B. Bischoff, A. Gurlo, M. Kunz, R.E. Dunin-Borkowski, S. Penner, M. Heggen, Atomic-Scale Insights into Nickel Exsolution on $LaNiO_3$ Catalysts via In Situ Electron Microscopy, J. Phys. Chem. C. 126 (2022) 786–796.
[34] S. Seetharaman, A. McLean, R. Guthrie, S. Sridhar, Treatise on Process Metallurgy, Elsevier,, Oxford, 2014.
[35] C.S. Fadley, Electron spectroscopy: theory, techniques and applications, in: C.R.Ba. A.D. Baker (Ed.), Electron Spectrosc. Theory Tech. Appl. 2, Academic Press, 1978.
[36] C.J. Powell, A. Jablonski, A. Naumkin, A. Kraut-Vass, J.M. Conny, J.R. Rumble, NIST data resources for surface analysis by X-ray photoelectron spectroscopy and Auger electron spectroscopy, J. Electron. Spectrosc. Relat. Phenom. 114 (2001) 1097–1102.
[37] G.A. Shafeev, J.M. Themlin, L. Bellard, W. Marine, A. Cros, Enhanced adherence of area-selective electroless metal plating on insulators, J. Vac. Sci. Technol. A 14 (1996) 319–326.
[38] K.S. Kim, A.F. Gossmann, N. Winograd, X-ray photoelectron spectroscopic studies of palladium oxides and palladium-oxygen electrode, Anal. Chem. 46 (1974) 197–200.
[39] A. Tressaud, S. Khairoun, H. Touhara, N. Watanabe, X-ray photoelectron-spectroscopy of palladium fluorides, Z. Anorg. Allg. Chem. 541 (1986) 291–299.
[40] H. Dropsch, M. Baerns, CO adsorption on supported Pd catalysts studied by adsorption microcalorimetry and temperature programmed desorption, Appl. Catal. A-Gen. 158 (1997) 163–183.
[41] C. Neyertz, M. Volpe, D. Perez, I. Costilla, M. Sanchez, C. Gigola, NO reduction with CO in the presence and absence of H_2O over $Pd/\gamma\text{-}Al_2O_3$ and $Pd\text{-}VO_x/\gamma\text{-}Al_2O_3$ catalysts: The formation of HNCO, NH_3 and stable surface species, Appl. Catal. A-Gen. 368 (2009) 146–157.
[42] T. Higo, Y. Omori, A. Shigemoto, K. Ueno, S. Ogo, Y. Sekine, Promotive effect of H_2O on low-temperature NO reduction by CO over $Pd/La_{0.9}Ba_{0.1}AlO_{3-\delta}$, Catal. Today 352 (2020) 192–197.
[43] D.G. Schlom, A.F. Marshall, J.T. Sizemore, Z.J. Chen, J.N. Eckstein, I. Bozovic, K. E. Von Dessonneck, J.S. Harris, J.C. Bravman, Molecular beam epitaxial growth of layered Bi-Sr-Ca-Cu-O, Compd., J. Cryst. Growth 102 (1990) 361–375.
[44] S. Rood, S. Eslava, A. Manigrasso, C. Bannister, Recent advances in gasoline three-way catalyst formulation: A review, Proc. Inst. Mech. Eng., Part D: J. Automob. Eng. 234 (2019) 936–949.
[45] E.G.M. Kuijpers, R.B. Tjepkema, W.J.J. van der Wal, C.M.A.M. Mesters, S.F.G. M. Spronck, J.W. Geus, Structure-sensitivity of the water-gas shift reaction over highly active Cu/SiO_2 catalysts, Appl. Catal. 25 (1986) 139–147.
[46] A.R. Balkenende, W.E.J. van Kooten, A.R. Pieters, M. Lamers, F.J.J.G. Janssen, J. W. Geus, XPS surface characterization of a Cu/SiO_2 catalyst oxidized by NO or O_2, Appl. Surf. Sci. 68 (1993) 439–444.
[47] Z. Wang, B. Li, M. Chen, W. Weng, H. Wan, Size and support effects for CO oxidation on supported Pd catalysts, Sci. China Chem. 53 (2010) 2047–2056.